

JOURNAL OF MECHANICS OF CONTINUA AND MATHEMATICAL SCIENCES www.journalimcms.org



ISSN (Online): 2454 -7190 Vol.-20, No.-11, November (2025) pp 30-54 ISSN (Print) 0973-8975

PLASMON FREQUENCY FOR ENHANCEMENT OPTICAL COMMUNICATION SYSTEMS

Aghssan Mohammed Nwehil¹, Husam Noman Mohammed Ali²

^{1,2} Laser and optoelectronics Technical Engineering Department, Al-Furat Al-Awsat Technical University, Engineering Technical College of Najaf, Iraq.

Email: ¹agsmohammed@atu.edu.iq, ²coj.husm@atu.edu.iq

Corresponding Author: Aghssan Mohammed Nwehil

https://doi.org/10.26782/jmcms.2025.11.00003

(Received: August 14, 2025; Revised: October 9, 2025; October 26, 2025)

Abstract

When properly excited at visible or near-infrared wavelengths, plasmonic materials display distinct with interesting appearances which could be overworked in the design and tuning of optical emission with diffusion settings at nanoscale scales. Researchers have presented a diversity of plasmonic heterostructures through scientific studies and used them to filter, transmit, detect, and detect light waves. And the amendment. In this study, implementations of modern plasmonic schemes utilized in communications are summarized. Their distinct roles have been discussed in multiple paths, including beam focusing, directing, filtering, modulation, switching, as well as reception, all of which are of paramount interest to the improvements of sixthgeneration (6G) cellular networks. An optical communications system has been simulated that simulates the implementation and use of plasmonic materials to filter optical waveforms and direct the communications beam in an efficient and focused manner while reducing the data reception error rate to an excellent rate to avoid noise waves and interference for the sixth generation.

Keywords: Plasmonics, Fiber Connectors, Nanoantennas, Optical Computing, Optical Detectors, Routers, Telecommunications, Filters

I. Introduction

Recent years have witnessed remarkable advancements in the utilization of the THz range, spanning from infrared to microwave frequencies, to accommodate the continuously increasing demand for enhanced data rates, significantly higher transmission speeds, reduced energy consumption, and improved integration of on-chip telecommunications performance. In this specific context, the significant potential of mineral nanostructures to capture and collect light at subwavelength scales has emerged as an innovative design. In contrast to their photonic (limited in size by diffraction constraints) and nano-electronic (subject to interconnection delays) counterparts, which transmit signals via photons or electrons independently, plasmonic modes represent electromagnetic signals that resonate with the collective motion of free electrons at metallic surfaces. Therefore, devices designed to counteract exceptional

data transmission rates of optical signals in photonic environments with miniature electronic circuits might be developed by the synergistic integration of photonic, plasmonic, and electronic domains on a chip [I-V]. In relation to the numerical parameters of metallic nanostructures, plasmonic resonances may encompass coordinated surface plasmon resonances (SPRs) or localized surface plasmon resonances (LSPRs), which will be analyzed subsequently. The activation and emission settings of LSPRs may be employed in distant optical connections, such as in the optoelectronic conversion of optical-to-THz and THz-to-optical transmissions for the planned filament compromise to-THz communication front-ends. Ultrafast board-toboard and chip-to-chip connections are advancing, and research is also being conducted on nanometric-scale analogs of radio frequency (RF) interconnects for operation in the optical domain. Despite these optical-remote micro connections, SPR characteristics can also be employed for plasmonic waveguides, transmitters, channels, and large switches [V-XV]. Surface plasmon resonances (SPRs) facilitate the resonant coupling of the electric field of light through free electron excitations in metallic coatings, thereby enhancing and concentrating light fields over considerable distances. Such rehashes can include multiplied (coordinated) or limited (emanated) surface plasmon resonances (LSPRs), depending on the numerical configurations of the metallic coating, offering a method for diverse integration of nanoscale near-field visual phenomena. Contrasts are not only found in inevitability and the qualities of radiation, but also, incidentally, it is stimulated. Localized Surface Plasmon Resonances (LSPRs) can be activated utilizing highly propagating light, but Surface Plasmon Resonances (SPRs) necessitate a comparably sensitive component to integrate the directly coupled light conditions, as illustrated in Figure 1 [X-XX].

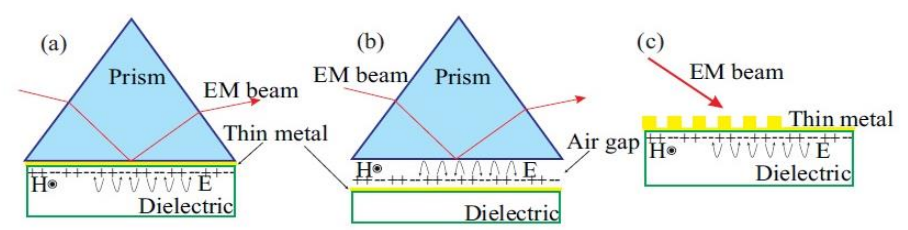


Fig. 1. Essential procedures to energize surface plasmon polaritons (SPPs): (a) The Kretschmann scheme, (b) Otto scheme, and (c) Grating matching. [VII-XVI].

Similar to the crystal coupler approach, such plasmonic grating designs have also been employed for sensing and biosensing applications. In transportation, they utilize space along communication cables for optical modulation systems. Concerning SPR approaches, LSPRs are activated by freely propagating light interacting with metallic nanoparticles or other discrete structures. In this scenario, the electric field's harmonic oscillation of light induces oscillations in the free-electron density within the material, akin to a restricted harmonic oscillator. The most significant dipolar peaks are identified when the frequency of light matches the typical frequency of electron density, known as the plasmon frequency (wp). These restricted and enhanced fields are typically employed for surface-modified characteristics in plasmonic biosensing applications [XIX]. The electromagnetic behavior of small and highly symmetric metallic nanoparticles can be well characterized using the semi-passive analogy. In

transportation implementations, LSPRs and SPRs are interdependently utilized to convert free emission into guided signals and vice versa. Prior scientific expressions hold subjective significance, while suitable theoretical analyses must be conducted using specific mathematical methodologies [XX-XXX].

I.i. Plasmoid Concept

Plasmon waveguides are structured devices designed to confine and amplify electromagnetic waves. Sub-diffraction borders are employed to transmit optical signals among diverse nano-optical circuits and their properties. These nanomodels can be manufactured by several distinct methods, including multilayer plates, nanoparticle configurations, metal-coated fibers, metal nanowires, and alloy networks, among others. Although these systems allow for exceedingly reduced connectivity latency in subfrequency scale devices, practical applications are hindered by power dissipation due to crosstalk among adjacent plasmonic waveguides [XXIV]. Specifically, ohmic losses occur in metals at critical optical frequencies with propagation distances of merely a few micrometers, prompting investigation into alternative propagation mechanisms. Recent evidence indicates that wireless data transfer at the nanoscale is a promising alternative. This methodology's communication execution is heavily dependent on the design of the associated nano-junctions, namely nano-transmitters and nano-receivers, utilizing RF antenna theory. We will examine the most recent strategies for highly efficient nanoantenna designs. The simplest nanoantenna component conceivable is a singular or dual alloy nanoscatter receiving wire (nano-dipole), as seen in Figure 2. The dispersion characteristics of these frameworks are extensively examined (from both mathematical and exploratory perspectives) as a consequence of engineering the nanoparticles with their respective impedance, indicating that they can be designed similarly to dipoles in the RF spectrum [VI-XV].

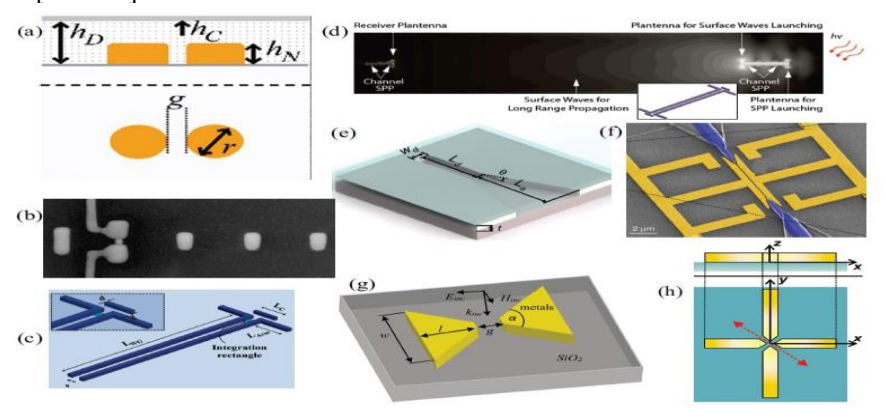


Fig. 2. Different and varied models of nanoantenna designs, (a) Dipole nanoantenna, indium tin oxide (ITO) coated, (b) Yagi-Uda plasmonic nanoantenna, (c) Plantina design type antenna, (d) antenna nanolink wireless communications, (e) Plasma horn type nano-antenna, (f) False color SEM micrographs of the formation of a little- also huge-frequency dual nanoantenna Plasmonic phase shifter (PPS) waveguide. (g) Unique nanotie. (h) Design of the asymmetric cross-sectional plasma antenna [VI-XV].

Figure 2 above shows different types of plasmonic nanoantenna designs, which appear in sizes and configurations that depend on the implementation and the working

frequency. The types of coatings and the nature of the alloy composition affect the efficiency of these antennas and the amount of gain achieved, in addition to the strength of the radiation guidance in transmission and reception.

I.ii. Plasmoid Modulators

Experts are seeking ultra-fast wireless THz links capable of seamlessly merging optical and THz (O/T) information carriers, while also addressing the increasing demand for elevated data rates in remote communication networks. In addition to the substantial potential of plasmonic nanoantennas discussed in the previous subsection, there are also other plasmonic antennas. Nanostructures provide superior performance and miniaturization for encoding information in the optical field by the deliberate manipulation of amplitude, phase, or both. This article surveys many promising methods for addressing waveform modulation using plasmonic devices. Figure 3a presents an illustration of a Mach-Zehnder Modulator (MZM). This principle employs dual gold strip waveguides embedded in the polymer, as illustrated. A portion of the strips is heated by power flows to create a phase disparity between the MZM dual arms, which subsequently alters the output adequacy [VI]. This modification technique has been effectively employed for waveform transmission at telecommunications frequencies ranging from 1.50 m to 1.61 m. Similar designs have also been proposed. Recently, the demand for practical ultra-fine silicon has also stimulated transmitters for on-chip optical and optoelectronic assessment devices. Additional approaches, including a metal oxide semiconductor (MOS) modulator for multimode interferometry in a plasmonic waveguide, have been proposed to enhance the frequency and increase the SPR electromagnetic field's electro-optical nonlinearity. The plasmon-based MOS modulation system, designated Marked PlasMOStor, is illustrated in Figure 3(b). The waveform dependent on PlasMOStor is transmitted by implementing rapid development limitations modulation in a MOS capacitor to achieve a modulation ratio of approximately 9.98 dB. Recently, the remarkable optical properties of graphene have prompted research interest in improving modulation performance, speed, and optical bandwidths. Multiple approaches exist to address graphene-based plasmonic modulation units, considering graphene as a capacitive dielectric double-layer intermetallic insulator (IMI) platform, as seen in Figure 3c. The produced graphene layers generate voltage, functioning both as a capacitor and a light shield, exhibiting electrical properties. It is designed to effectively modulate the signal [VI, XIX].

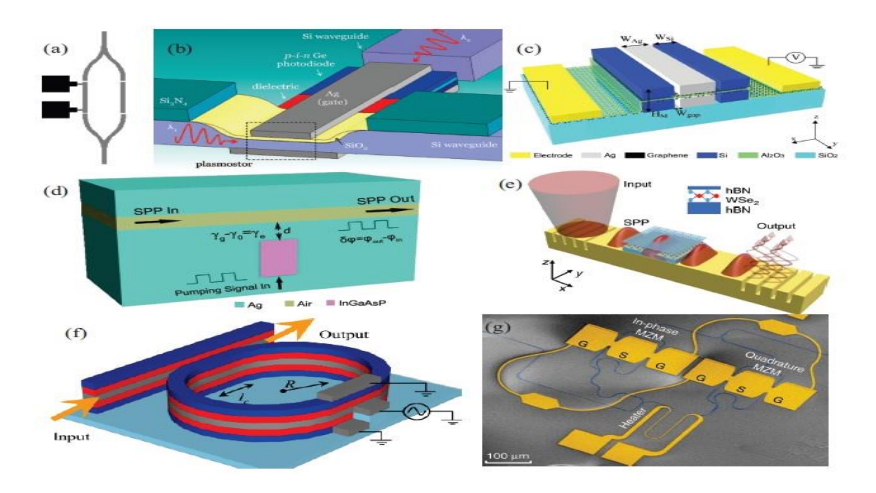


Fig. 3. Various models of nano-embedded designs of different shapes and sizes and implementations, A) Shows a perspective on the Y-Shape Mach-Zender Modulator (MZM). (b) Graphical drawing of all optics Plasmonic metal oxide semiconductor (MOS) modulator. (c) Photography of a metal-insulator Graphene-relied dual-opening plasmonic waveguide transmitter. (d) Schematic demonstration of a plasmonic metal-insulator (MIM) waveguide paired to a plasmonic square shape vibrator. (e) Graphical sketching of 2D hBN-WSe2-hBN (hexagonal boron nitride-tungsten) Diselenide -hexagonal boron nitride) semiconductor on grid mixer-relied plasmonics Waveguide for exciton-SPP coupling. (f) Demonstration of the horizontally half-and-half plasmonic waveguide mixed with a plasmonic ring vibrator. The dual frameworks are operated as silicon-EOP-silver-EOP-silicon Multilayer on SiO2 substrate. EOP -electro-optic polymers. (g) Bogus variety SEM micrograph two uneven rapid plasmonic MZMs compacted toward the Taste MZI. [VI-X].

Figure 3 illustrates a variety of plasmoid nanostructure modulators employed for different frequency bandwidths and applications. The design structure, dimensions, building materials, and features will vary for each scheme based on the implementation and pattern acquisition. Figure 3(a) presents an overview of the Y-Shape Mach-Zehnder Modulator (MZM) type, whereas Figure 3(b) illustrates a graphical representation of the complete optical plasmonic metal oxide semiconductor (MOS) transmitter. Furthermore, Figure 3(c) presents an image of a metal-insulator graphenebased dual-opening plasmonic waveguide transmitter, while Figure 3(d) illustrates a schematic representation of a plasmonic metal-insulator (MIM) waveguide coupled with a plasmonic square-shaped vibrator. Additionally, Figure 3(e) illustrates a schematic representation of a 2D hBN-WSe2-hBN (hexagonal boron nitride-tungsten) semiconductor integrated with a grid coupler-based plasmonic waveguide for excitonsurface plasmon polariton coupling. Figure 3(f) depicts a horizontally bisected plasmonic waveguide integrated with a plasmonic ring resonator. Moreover, the two frameworks function as a silicon-EOP-silver-EOP-silicon multilayer on a SiO2 substrate. Electro-optic polymers (EOP). Figure 3(g) presents a Bogus variation SEM micrograph including two irregular fast plasmonic MZMs incorporated into the Taste MZI [VI-XV].

I.iii. Surface Plasmon Resonance Fiber Optics Mixture

Indeed, the aforementioned indicates that surface plasmon resonance (SPR) is an optical method employed to assess molecular interactions in real time. Surface Plasmon Resonance (SPR) can arise when polarized light impinges upon a metallic coating under conditions of total internal reflection. The SPR waveform is directly contingent upon the refractive index of the channel on the sensor chip. The components of Surface Plasmon Resonance (SPR) are a light source, an input system, a prism with an analytical interface, a detector, and a computer. The primary chemical constituents employed in the fabrication of optical fibers are silica (silicon dioxide), analogous substances (including germanium, phosphorus, or boron), and diverse coating materials. The criteria for Plasmon configuration, regarding performance and installation, closely resemble those of fiber specifications, and all parameters and measurements for Plasmon may be calculated based on the operational standards of optical fiber. Therefore, the measurements of fiber optics include losses, attenuation, bit error rate (BER), transmission quality factor (Q), signal-to-noise ratio (SNR), power budget, and total transmission time. Consequently, the maximum spectrum response losses associated with fiber optic cable characteristics may be demonstrated to correspond with the losses of plasmonic components. The extent of losses and transmission attenuation is contingent upon the light repetition procedures and the composition of the fiber alloy. The loss rate can be calculated using the following equation [XIX-XXV]:

$$Loss(dB) = -10 Log \frac{P_{out}}{P_{in}}$$
 (1)

Where Pin is the entered power to the fiber, P_{out} is the power resulting at the fiber outlet. Also, one could calculate the amount of attenuation (measured in decibels per kilometer (dB/km)) that occurs in optical fibers through the incoming mathematical expression of:

$$\alpha(dB/Km) = -\frac{10}{L} Log \frac{P_{out}}{P_{in}}$$
 (2)

To such a degree that α represents the attenuation coefficient. The "optical fiber" may be classified as either single-mode (SM) or multimode (MM). A multimode fiber is utilized over short distances; these fibers possess high capacity and reliability. The primary distinction between single-mode fiber and multimode fiber is that multimode fiber possesses a larger core diameter and a significantly higher numerical aperture. Consequently, the light-collecting cutoff of the fiber is substantial. In multimode fiber, the data transmission distance is significantly less than that of single-mode fiber due to the presence of many propagation modes. The attenuation coefficient (a) for singlemode (SM) fiber is less than that of multimode fiber (MM). Similarly, a fundamental constraint characterizing the concept of input interfaces is the error rate. The Bit Error Rate (BER) facilitates the consideration of diverse systems for information communication. Nonetheless, the Q-factor represents the concept of a significant signal from a fundamental perspective. The Q-factor and Bit Error Rate (BER) are the primary determinants that limit the transmission range in optical communication models. To transmit messages over extensive distances, it is essential to maintain a low Bit Error Rate (BER) with a high Quality factor (Q-factor) within the fiber. The Q-component

may be utilized to induce a detrimental influence on the Bit Error Rate (BER), and the correlation between the Q-factor and the error rate may be articulated as follows [VI-XX]:

$$BER = \frac{1}{2} erfc(\frac{Q}{\sqrt{2}}) \approx \frac{1}{Q\sqrt{2\pi}} exp(-\frac{Q}{2})$$
 (3)

Where erfc indicates the amount of interconnected hard effort. The Q-factor might be corresponded as far as the electrical waveform to-noise ratio (SNR) by the expression:

$$Q = \frac{SNR\sqrt{2TB_{opt}}}{1+\sqrt{1+2}SNR} \tag{4}$$

Such that, T is the bit time and B_{opt} is the rectangular optical filter bandwidth. Also, the SNR is a metric utilized in engineering knowledge and to determine how much a wave is affected by noise. It is outlined as the proportion of the waveform strength to the noise strength that corrupts the data waveform, and it can be computed through the following relationship:

$$SNR = \frac{I_1 - I_0}{I_0} \tag{5}$$

In which I_0 and I_1 are the means of the amount of low-pass filtered electrical currents at the time of sampling, lengths, and variables [VI-XV].

The power ought to be adequately high to sustain the BER to a minimum value; of course, the achieved energy must be under enough to prevent the system damage. The essential energy required could be determined by finding the supporting energy expenditure model to measure the fiber length, attrition, and fatigue in the connectors and splices. The power spending design could be represented as follows: [VI-XX]

$$powerbudget(dB) = Ptx[dB] + Pmin[dB]$$
 (6)

Referring to relationship (6), the capacity expenditure design depends on the transmitted energy, which is the basic power that is expected to perform basic information transmission and improve BER rates. Through the use of the energy consumption design, it is possible to know the state of permissible throttling in the overall process of communications and information transfer, and this overall throttling tends to narrow in the optical fibers transmitted in terms of (dB/km), even though the amount of attenuation is due to the relationship shown in equation (7):

$$\alpha_{fiber}L + \alpha_{coupling}N \le powerbudget[dB]$$
 (7)

Where L denotes the fiber length, and N represents the fiber coupling nodes. Hence, by looking at Equation (7), one can notice that the power budget construction should be higher than or equal to the amount of attenuation losses resulting from the length of the optical cable combined with the coupling attenuation losses. Figure 4 demonstrates the relation of power transmission against fiber optical cable layers [V-XVI].

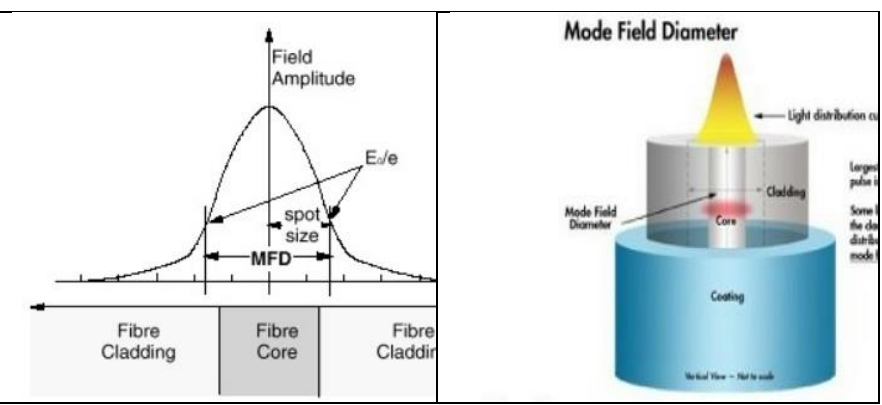


Fig. 4. Demonstrates the relation of power transmission against fiber optical cable layers [VI].

Figure 4 shows the mechanism and form of energy transmission and the direction and concentration of the power of light radiation through the layers of the optical wire. We observe that most of the energy is concentrated at the center and core of the optical carrier, while a small percentage is directed to the sides and cover of the optical cable, which indicates the importance of isolating the center of the core from the external environment, which is directly proportional to the efficiency of concentrating and transmitting energy along the path of the fiber optic cable.

Also, the total waveform flow time rate can be evaluated in terms of the communication time inside the optical wire, along with the transmission and reception times, as shown in the relationship below:

$$\Delta t_{overall} = \sqrt{\Delta t^2_{transmitter} + \Delta t^2_{receiver} + \Delta t^2_{fiber}}$$
 (8)

From the equation above, it can be seen that the general reaction time is the square root of the quadratic summation of the riser period of the transmitter and the riser instant of the receiver, in addition to the propagation period of the pulse resulting from the dispersion of the fibers. Sender, recipient, with complete rise instants are recorded on data covers. Fiber interaction periods should be determined from the fiber distance, the information dispersion per unit length, and the width across the optical cable. In fact, there are three types of diffusion: typical, chromatic (it is the amount of matter and waveguide diffusion), and polarization mode diffusion. In single-mode threads, the standard diffusion is zero. However, chromatic diffusion and dispersion in the polarization mode are crucial. The bandwidth of a fiber optic exchange system is the absolute simple transmission speed or rate of information it can transmit. With frequency division multiplexing, the fiber limit is the limit amount of every optical medium supported by the fiber. For reasons of cost and safety, it is considered acceptable to sustain the modulator power at a minimal transmitter power and, likewise, choose a modulator light supply having adequate energy to correspond to the model in operation under the noisiest case limitations against maximum noise and effects. Furthermore, the design must take into account some additional features over the recipient's basic requirements for architecture advancement considerations, variations, and fixes. Also, the interest components are the refractive index n, the group index ng,

as well as the group speed dispersion D. The refractive index of clear silica in the wavelength range from 199 nm to 3.99 μ m is produced by the incoming experimentally installed Sellmeier relation [VI]:

$$n^{2} = 1 + \frac{0.7\lambda^{2}}{\lambda^{2} - (0.07)^{2}} + \frac{0.408\lambda^{2}}{\lambda^{2} - (0.117)^{2}} + \frac{0.9\lambda^{2}}{\lambda^{2} - (9.9)^{2}}$$
(9)

Such that, λ represents the wavelength signal in μ meters. The refraction index might be varied by summing dopants to silica, such that simplifying the averages to adjust the fiber index shape. Thus, as mentioned above, Fiber diffusion outcomes in optical pulses, also expanding digital signal decay. Also, an increase in the error's sum might be shared on the digital optical medium as the ISI becomes further cleared. The enhancement in plasmois–based fiber transmission is evident in the structured spectral response and guided energy distribution. Chromatic dispersion within the optical fiber induces pulse broadening, which in turn degrades signal fidelity, limits transmission reach, and necessitates compensation mechanisms to maintain communication quality. For Dense Wavelength Division Multiplexing DWDM models employing Distributed Feed Back Laser DFB lasers, the ultimate link distance prior to being impacted by chromatic diffusion is commonly computed with the following formula [VI-XX]:

$$n^2 = \frac{104,00}{CD.L} *B^2 \tag{10}$$

Where L is the channel range in km, CD is the prismatic diffusion in (peco sec)/(nm * km) units, and B is the bit rate in Gbps. Thus, the formation of an optical fiber with ultimate reflectivity with graphene can be deduced through the diagram shown in Figure 5, indicating the reflectivity with respect to the wavelength [VI-XX].

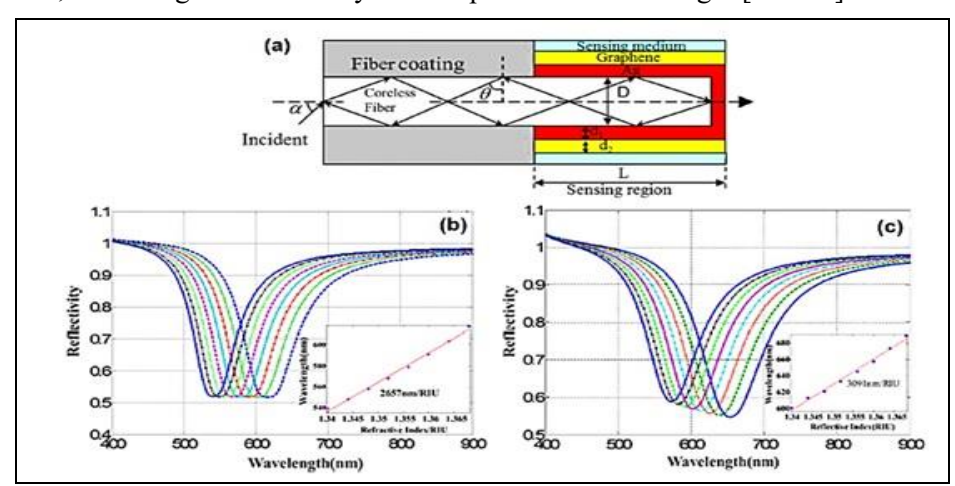


Fig. 5. The formation of an optical fiber with ultimate reflectivity with graphene, (a) Schematic diagram, (b) The sensitivity spectra and reflectivity with respect to the wavelength without graphene, (c) With graphene [VI-XX].

Surface plasmon resonance (SPR) biosensors have evolved into a really effective perceptive tool. Studies of biomolecular interactions. One can excite a surface plasmon in several methods, for example, Advancing such sort is tested in coupling with a

crystal, optical fiber, network, nanoparticles, and so on. The biosensor is gaining more sensitivity. Among the now-used materials is graphene. Considering its unique qualities, it has been generally discussed. Many studies have shown this material to tentatively and theoretically forward the SPR sensitivity. A few important studies are discussed on the improvement of a graphene-reliant SPR biosensor for various activation techniques. Talks on the general graphene characteristics and their use in biosensors open the conversation. For several methods, implementation and test results are described. Furthermore, extending the discussion on SPR biosensors is a survey on graphene-reliant biosensors. Surface-upgraded Raman scattering (SERS) generates an outline of future material evolution in the biosensor [VI-XIX].

One of the key benefits of an SPR sensor is real-time biomolecular binding interaction monitoring. One might just track in real time the attachment and dissociation of molecules. Consequently, SPR fiber optical sensors might be modeled by the robust micro-electromechanical vibrator (MEMS) model, with acquired impedances and frequencies under the effect of % frequency change. Beneath the effect and influence of a designated percentage change in the designed resonance frequency, f_p , the proposed vibrator frequency designed values, as well as the related vibrator impedances, C_o , C_m , L_m , and R_m have been designed. Simulated with the ramp function r(t), this percentage change generates designed vibrator impedances as well as recorded resonance frequency changes. This model will investigate how MEMS vibrator performance is affected by the % change in the resonance frequency. Actually, one further supporting modeling relation could be used to represent the operation of the SPR sensor to ascertain the band pass filter equivalent spectra, f_s and f_p , against the BPF quality variable, Q, that could be obtained by means of relations based on FBAR band pass filter construction.

$$\epsilon = \frac{z_{Acoustic}}{v \times D} \tag{11}$$

$$f_{p} = \frac{V}{h} \tag{12}$$

$$f_s = 0.85 f_p$$
 (13)

$$Q = \frac{f_s \times d}{0.05 \times f_n \times A} \tag{14}$$

Such that, Z_Achoustic is the FBAR audio obstruction or impedance, V is the FBAR audio speed, D is the piezoelectric substaintial stiffness, also d is the thickness of the slim film FBAR deviation. As it is clear through the above relations, the real FBAR density - film materials boundaries would decide the bandpass filter plan procedure.

The remaining organization of this article will be as follows. Section 2 will present the most modern and important studies and scientific articles concerning the issue of plasmon frequency for enhancing optical communication systems, as related works. The methodology of this paper will be discussed in Section 3 with simulation design details and a procedure flow chart. Section 4 will introduce the simulation results with a comprehensive discussion and comparisons. Finally, conclusions will be outlined in Section 5.

II. Related Studies

While indicating the degree of their efficiency and benefits in comparison to the difficulties, obstacles and challenges (research holes), one could summarize the main works and contributions of specialists and researchers to the most prominent strategies and technologies that employ them by means of what has been achieved in scientific research and recent studies in the field of using plasmons in optical communications, evaluated in this part. Investigating the effect of a one-stage graphene layer on SPR sensitivity in end-intelligent optical fibers using a dull fiber measurement of 600 µm Zhou et al., [XXXIII], the silver has 40 nm of thickness. This was shown in refraction. The sensitivity of SPR beyond as well as employing graphene was 2657 nm/RIU and 3091 nm/RIU, respectively; the index ranged from 1.3411 to 1.3737. Results of implementation confirm that graphene in conventional optical fibers has been shown to increase sensor sensitivity. Chiu et al., [VII] conducted an exploratory study of another strategy in 2018—more precisely, GO-reliant Models functionalized with - COOH (GO-COOH chip) as a resistant sensor for non-little cell cellular breakdown in the lungs detection by cytolytic 19 (CK19). Estimates of biomolecular interactions between CK19 and against CK19 at different doses, continual learning of sensor data for every produced chip. Based on sensor data, the GO-COOH-based SPR chip has a further limited performance duration than the usual device. Running - COOH on GO also produced a better recognition cutoff of -0.001, 100 pg/ml. Basak, C., et al. looked at how a graphene layer affected an alternate significant—more precisely, Silver—in 2020. One drives a higher reflectivity at SPR point and shallower SPR bend by increasing the graphene layers. Furthermore, the abatement in sensitivity makes it impossible to get away from an increase in the graphene layer amount. Still, it should be somewhat similar. The presence of a graphene monolayer and bilayer in the SPR biosensor offers a major breakthrough in SPR sensitivity. The SPR sensitivity in such construction is 3.5 against 2.5 times higher than in typical gold-relayed biosensors. Zhu, L., et al., [XV] examined the idea of an H-molded photonic gem fiber in 2020. U Shape SPR biosensor Furrows provide an open architecture for refractive index sensing. Photonic gem fiber (BCF) is another form of optical fiber used in SPR biosensor implementations. Made from PCF, biosensors have their air vents arranged hexagonally in two layers. Against the plasmon mode, the central air outlet can reduce the suitability RI from major to phase orientation. Two large air holes exist. In the main layer, which causes the phenomena of strong polarization and strong double refraction, Light contacts the metal-insulating interface. 2019 saw Huang, et al. [XI] present a single-mode-multimode multifiber (MMF) mode. For the heat sensor (SMF-MMF), graphene compounds covered the body. Sensor uses polydimethylsiloxane (PDMS) as the heat cushion sensor; the addition of center shell gold and silver nanoparticles (Au@AgNPs) considerably enhanced the sensitivity. PDMS is a material having a high optical thermal coefficient (±4.5 10-4/C) whose refractive index reduces with increasing heat. Investigate momentarily, Figures 15a show the cycle. Figure 15b displays the biosensor's reaction over several temperatures. The SPR frequency changes on a small scale as the heat rises. As the heat changed, the SPR frequency swung from 851.41 nm to 798.60 nm. Between 30°C and 110°C. Sadeghi and Shirani [XX] conducted research in 2020 with an eye toward mid-infrared display of a graphene and gold grating SPR sensor. One may see a schematic outline of the studied

biosensor here: Proposal Nanostructures Starting limits of the SPR biosensor. They also studied how the SPR biosensor responded to rectangular grids. This model's sensitivity results have been recorded to be 1180 nm/RIU. In 2018, Chiu et al. [VII] proposed a colorimetric LSPR immunoassay considering an AuNPs-GO half breed. To separate disease biomarkers and instantly identify infectious diseases. Connection Monitoring changes in optical absorption helped AuNPs-GO-hostile to BSA be identified as GO-BSA. At a given frequency. Two absorption tops with frequencies 540 nm and 760 nm exist. From this absorption top, one derives a calibration bent displaying the link between absorption change and hostile to BSA concentration. Two pinnacles define the height. By use of a Linear reach from 145 FM to 1.45 nm, this sensor detects the furthest reaches of 145 fM. Furthermore, showing a synopsis of the contemporary research papers examined on the SPR biosensor utilizing fiber optical sensors [X-XXX] are Tables 1, 2, and 3.

Table 1: Summary of the modern research articles that investigated the SPR biosensor against fiber optical sensors [X-XXX]

Fiber optic Type		Structure		Target	Sensitivity and Limit of Detection (LOD)	
Side polished optical fiber		Au/graphene		ssDNA	1039.8 nm/RIU and 10 ⁻¹² M	
Plastic clad silica fiber		Au/graphene		BSA	6500 nm/RIU	
Plastic clad si	lica fiber	Au/graphene		BSA	7.01 nm/(mg/mL)	
End reflection of	ptical fiber	Ag/graphene		NaCl solutions	3936.8 nm/RIU	
U-bent plastic optical fiber		Graphene + Ag nanoparticles		Glucosa solutions	700.3 nm/RIU	
MMF-PCF-MI	MF sensor	Au+graphene+SPA		anti-human IgG	4649.8 nm/RIU	
D-shaped fiber		Cr/Au/MoS2/graphene		Glucosa	6708.87 nm/RIU	
Grating	shape	Struct	ure	Analyte	Sensitivity	
Rectangular		Au/graphene		dangerous gases	1180 nm/RIU	
Ellipse		Au/graphene		Biological cells	1782 nm/RIU	
Rectangular		SiO ₂ /graphene		ssDNA	8004 nm/RIU	
Holey		Au/graphene		Ethanol	-	
250		ra/ graphene		Litation		
Long period fiber grating (LPFG)		Ag/graphene		Methane	0.344 nm/%	
Rectangular		Ag grat- ing/Ag/graphene		51	220°/RIU	
Technique	Str	ructure	Analy	te Sensitivity	LOD	
SPR	DATE SECTION	rs of GO-Au composite	miRNA-	141 -	0.1 fM	
LSPR		GO-anti BSA	hCG	1170	145 fM	
SPR	nanohy	Au-(Au NPs-Graphene nanohybrids)-anti		gG	0.15 μg/mL	
LSPR	human IgG Au NPs coupled with GO		NO ₂	92	20	
SPR	Graphene-coated SPR with Au nanostars		ssDNA	4 -	500 aM	
LSPR	carrying ssDNA Au NPs/GO/uricase		Uric ac	id 0.0082 nm/µ	Μ 206 μΜ	

III. Proposed Model Methodology

In this Section, the methodology of the proposed face features model will be presented and illustrated in detail. In this study, the essential technique that has been suggested to implement the SPR model requirement which might be implemented using the Film Bulk Acoustic Resonator (FBAR) scheme. The FBAR is a Broadcom's version of piezoelectric filtering for bulk acoustic waves (BAW) as illustrated in the literature. In this project, the proposed SPR model of the study will be discussed in detail, against the scheme that was implemented according to the Micro-Electro-Mechanical System Vibrator (MEMS). The suggested design lab system model will simulate the SPR scheme using the MatLab2020b Simulink toolbox for modeling the required FBAR band-pass filter design parameters values. In this study, a planned system is proposed for robust and efficient monitoring against control design for a micro-electromechanical vibrator system.

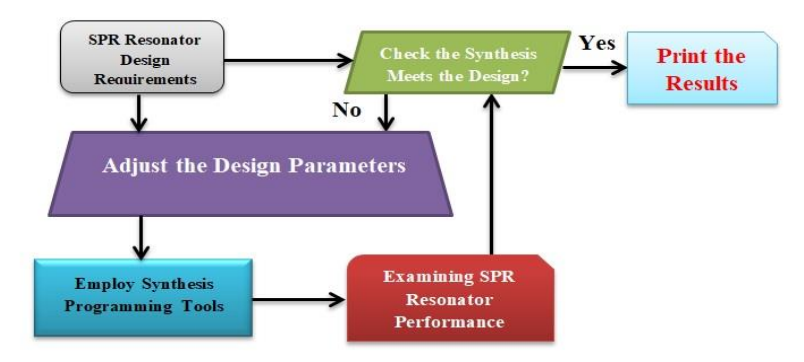


Fig. 3.1. Block diagram of the planned SPR vibrator model.

The block graph of the arranged hearty microelectromechanical resonator (SPR) framework model. The items in this proposed model construction will consist of six principal block graphs. The principal block graph is the vibrator design prerequisites, which will be mindful of starting the fundamental necessities and requests of the construction frequencies on impedances of the MEMS vibrator. The subsequent block outline will be known as the arrangements of design boundaries, which will be dependent on setting and changing the design boundaries, and supporting the electronic materials. The third block outline which will be shown by the blue tone is known as the amalgamation programming apparatus, this will be mindful of programming the product expected for having control of all the proposed model in this model will be called analysing the exhibition got by the combination and tried to check in the event that the construction boundaries of the frequencies on the impedances of the resonator have been changed. For changing the activity in the effective design area and reach. The fifth block outline in this proposed model will be known as actually taking a look at the examination or inspecting the union design, and it will have two sections; the main will be accessed if the construction boundaries are alright. At the point when the outcomes are yes, then the outcomes will be printed. If no, feedback to the subsequent block chart, which is known as the arrangement of the design boundaries, will be received to overhaul the boundaries, and the general cycle will be repeated until the outcomes are acquired in exact and accurate qualities.

III.i. Design Details

The individual self-test model has been proposed to perform a robust microelectromechanical vibrator system. Such a self-test technique was additionally utilized for the frequency adjusting process. A block diagram of the self-test FBAR proposed scheme is displayed in Figure 6.

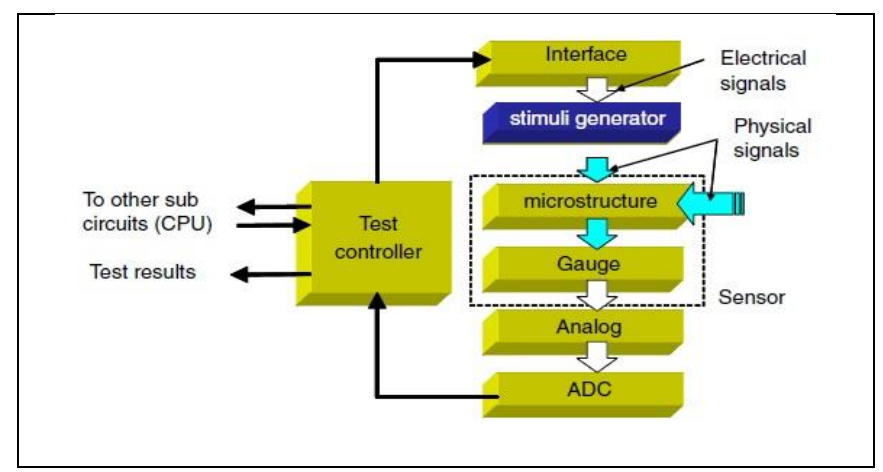


Fig. 6. Block diagram of the self-test SPR-based FBAR suggested model.

To implement the suggested scheme, illustrated in Figures 5 and 6, has been simulated by utilizing MatLab2020a Simulink program, which produces an efficient toolbox library necessary to satisfy the design requirements. Figure 7 illustrates the MatLab2020b Simulink design of the suggested design lab system model.

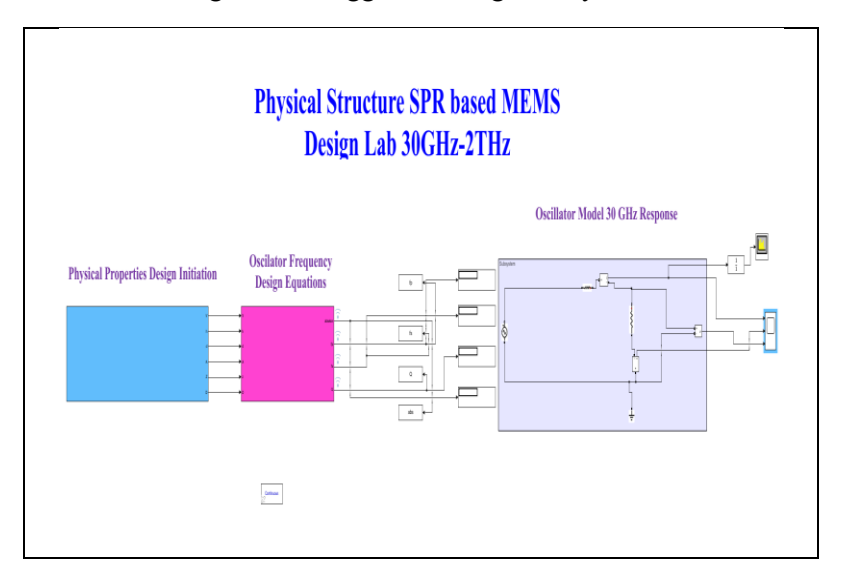


Fig. 7. MatLab2020b Simulink design lab system model utilized for SPR-based FBAR parameters design.

The above model system consists of three main subsystems as follows: 1) The Design Lab, 2) The SPR-based FBAR formulas, and 3) The SPR-based FBAR Circuit. Every subsystem delineated in Figure 8 will carry out a particular task important to finishing the general FBAR bandpass filter design prerequisites. The main subsystem is displayed in Figure 8, it will be important to instate the FBAR piezoelectric physical boundaries design values, for example, the acoustic speed, V, thin-film thickness, h, acoustic impedance, Z, piezoelectric physical density, D, thin-film region, A, and the thin-film thickness deviation, d. The subsequent subsystem displayed in Figure 3.4b, will be important to design the FBAR band-pass filter required series resonant frequency, equal resonant frequency fp, and the quality component, Q. At long last, the third subsystem showed in Figure 8, will be vital for design the last FBAR band-pass filter inward impedance boundaries like the Co, Cm, Lm, and Rm. The last registered FBAR band-pass filter values will be shown utilizing the MatLab2020b Simulink show instrument from the upheld library. To understand the SPR-based FBAR-based bandpass filter fiber optical model, there ought to be two arrangements of FBAR resonators, whose equal reverberation repeat of one set ought to be identical to the sires' reverberation repeat of the other pair. The possibility of the individual test proposed model actuator is summed up by alluding to the model displayed in Figure 9, using the end goal that the MEMS vibrator will set the design according to the physical boundary determinations of the piezoelectrical materials provided by the combined programming block. The subsequent MEMS-designed boundaries will be inspected through the use of the SPR-based MEMS block, and afterward the results will be contrasted and the genuine outcomes delivered by the first MEMS resonator block. At last, in the event that the examination results are not coordinated, the design set technique will be rehashed; otherwise, the outcomes will be printed. To carry out the proposed model, a MatLab2020b simulation program has been applied using the Simulink tool and component utilities. Figure 8 represents the simulation of the proposed model using the MatLab2020b Simulation software.

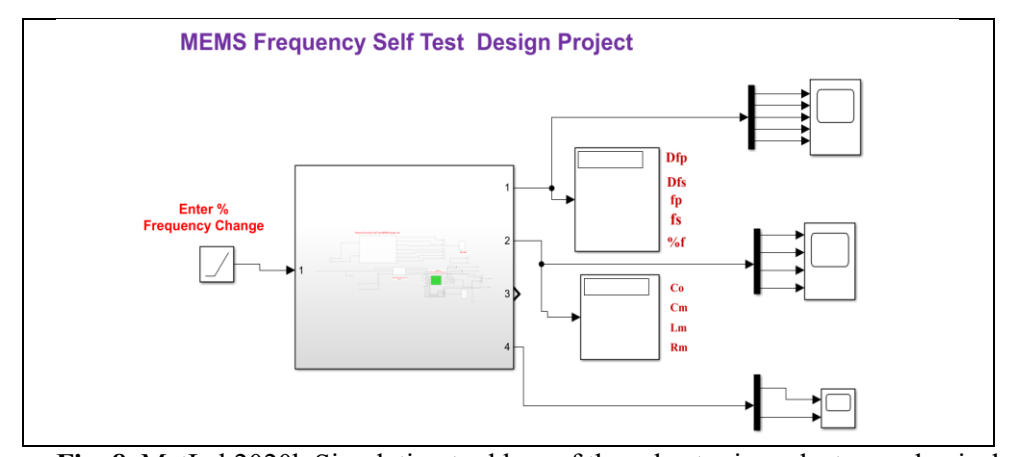


Fig. 8. MatLab2020b Simulation tool box of the robust micro electromechanical resonator SPR scheme.

Table 3.1 illustrates the design parameters utilized in the design program against the obtained FBAR filter resulting parameters for a cutoff frequency of $f_c=1.7\sim2$ THz.

Table 1: Design Parameters vs. Resulting FBAR Filter Values for Cutoff Frequency fc=1.7 \sim 2 THz

Parameter	Design Value	Resulting FBAR Value	Unit	Remarks	
Acoustic Velocity V	5200	_	m/s	Determines the central resonant frequency	
Thin Film Thickness h	1.5×10^{-6}	_	M	Key to adjusting frequency	
Deviation d	3.5×10^{-3}	_	M	Alters Q-factor	
Area A	3.5×10^{-4}	_	m²	Affects impedance calculations	
Impedance Z	20	_	Ohm	Acoustic impedance	
Density D	1.25×10^{8}	_	kg/m²	Material property for filter calculation	
Series Resonance fs		1.7 × 10 ⁹ \sim 1.7×10 ¹²	Hz	Output from simulation	
Parallel Resonance fp	_	2 × 10 ⁹ \sim 2 ×10 ¹²	Hz	Output from simulation	
Quality Factor Q	Calculated via Equation (14)	Varies per fs and fp	_	Directly impacted by design deviations.	

Table 2: Construction components used in the simulation, along with the achieved SPR-based FBAR filter resulting components using f_c =2 GHz to 2 THz.

SPR/FBAR Components	V Acoustic Speed (m/s)	h SPR/FB AR stiffness (m)	d SPR/FB AR stiffness deviation s (m) 3.5e-3	A SPR/FB AR area (m2)	Z_achoustic Acoustic Impedance (Ohm)	D SPR/FB AR Density (Kg/m2)		
0 (77.)	3.203	1.50-0			20	1.2300		
fp (Hz)	2 e9 to 2 e12							
fs (Hz)	1.7 e9 to 1.7 e12							

It is obvious from the design conditions Table 2 and alluding to the got SPR based FBAR design boundaries, that the optical vibrator cutoff series and equal frequencies will essentially rely on the acoustic speed, V, of the piezoelectric materials too on the thin film thickness, h, Moreover, the worth of the quality element will be changed by the varieties in the designed SPR based FBAR frequencies. Additionally, the stream diagram of the by and large proposed SPR-based MEMS design method is displayed in Figure 9.

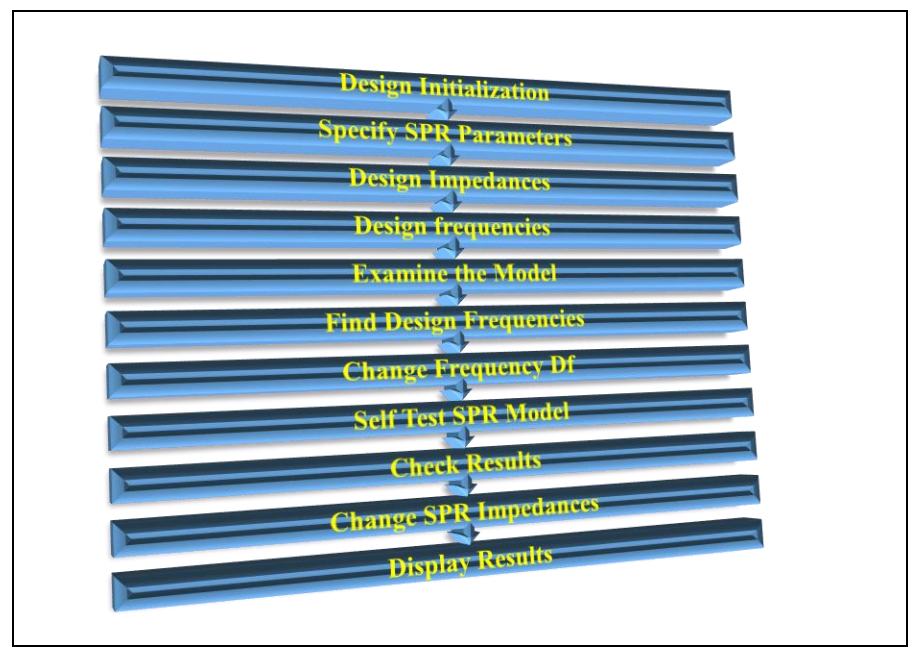


Fig. 9. The flow chart of the overall proposed SPR-based MEMS design procedure.

By reviewing the details of the flow chart for the steps of designing and implementing the proposed model shown in Figure 9, the design begins with preparing the fundamental requirements, such as the values of the internal impedances representing the performance of the internal configuration of the proposed model of the optical plasmon transmitter based on the piezoelectronic properties of the MEMS model. After that, the values of the design impedances and the amount of change in them are called into the design model to implement it according to the descriptive and equivalent equations to perform its work to extract the required frequencies. This is followed by displaying the results and plotting them in the time domain, then adding a partial change to the frequency values and re-executing it by calling the self-test design model to find the amount of changes occurring in the values of the internal impedances equivalent to the optical model. After this step, the results of the equivalent impedances evaluated as a result of the changes are shown, as well as their comparison against the changes in the design frequency values of the proposed plutonium optical transmitter. The results are verified and re-executed until the required values are reached, which achieves high accuracy and minimal error, and then the results are displayed and plotted.

III.ii. The Implemented Dataset

In this study, the data sets utilized in the proposed model are prepared using MATLAB tool libraries. The data set is represented by the values of parameters and variables of ferromagnetic materials that make up the proposed model for plasmonic optical transmission based on FBAR and MEMS schemes. Figure 10 shows the sources of the data set processed for the proposed SPR based MEMS design model.

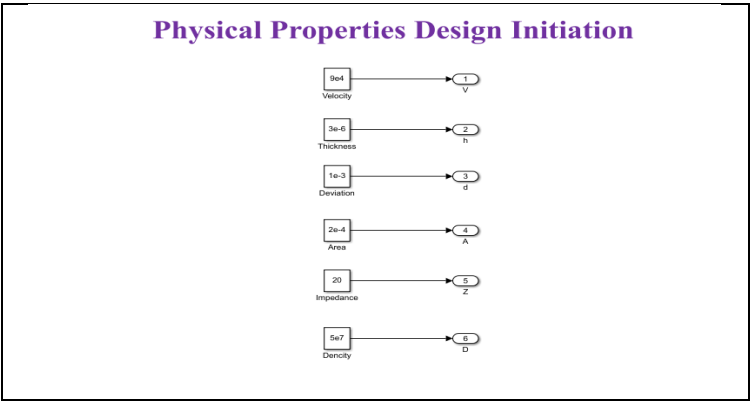


Fig. 10. The sources of the data set processed for the proposed SPR based MEMS design mode.

By looking to Figure 10, it is obvious that the dataset will be achieved by providing the initial values of the waveform velocity (v), the substrate thickness (h), the nanomaterial wavegude deviation (d), the fabricated area (A), the overall internal impedance (Z), and the peozoelectronic material density (D). in fact the values of these parameters which denoting the model dataset will adjust the suggested model design and utilized to evaluate the model SPR based MEMS internal impedances, Cm, Co, Lm, and Rm.

IV. Simulation Results

In this Section, the methodology of the proposed SPR fiber optical model will be implemented utilizing MatLab2020b m. files, script codes, and based on FBAR and MEMS models. The essential suggested technique of the SPR model, which has been simulated to implement the high-quality fiber optics communications model requirements, and simulated with the design parameters and nanostructure quantities specified in Table 2. The suggested models introduced in Figures 8, 9, and 10 have been strongly planned, programmed, and employed against the planned particulars introduced in Table 2. The results will be displayed in the form of text boxes with labels defining the state of the human face features, as will be illustrated in the incoming paragraphs.

The percentage change in the planned frequency has been updated to 0-50%, and examined strongly, with the achieved self-test SPR-based MEMS resonator frequency alternations amounts as shown in Figure 11.

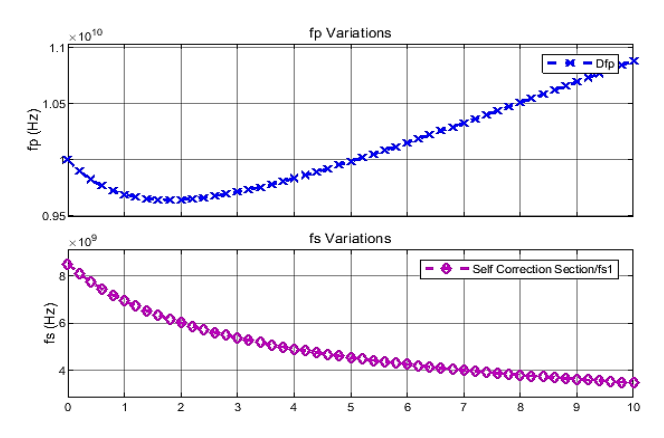


Fig. 11. Results of the self-test SPR-based MEMS actuator frequency changes to percentage frequency variations with time.

As presented in Figure 11 above, the resulting self-test SPR-based MEMS actuator frequency variations amount to Δf_p and Δf_s will be as a percentage ratio of the actual designed frequencies f_p , and f_s and are linearly increased with the increased percentage ratio. Also, for the same percentage variation in the designed frequency fp, as it is clear from Figure 11, the variations in the designed parallel and series frequencies f_p , and f_s , have been changed in almost a linear relation for linear percentage change in their values. Furthermore, the resulting self-test SPR-based MEMS actuator impedance parameter variations are displayed in Figure 12.

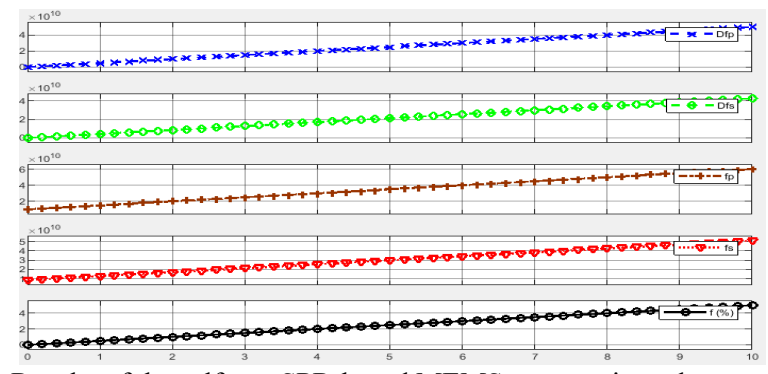


Fig. 12. Results of the self-test SPR-based MEMS actuator impedance parameters response to percentage frequency variation with time.

By referring to Figure 12, the percentage change in the designed frequencies will be examined upon the resulting SPR-based MEMS actuator impedance values. It is obvious that, there the initial and motion capacitances of the MEMS actuator will not be affected by these variations since their design model is independent of the operating MEMS frequency. While the motion inductance and resistance of the MEMS actuator are highly inversely dependent on the percentage variations in the operating designed frequency. This is due to the high dependency on the structural characteristics of the MEMS Lm and R_m impedances, which are highly affected by the frequency variation, especially the motion inductance, L_m , that might reach zero value for a 50% increasing

change in the operating frequency values. Moreover, the results of the proposed self-test SPR-based MEMS model have also been extracted and plotted as presented in Figure 13.

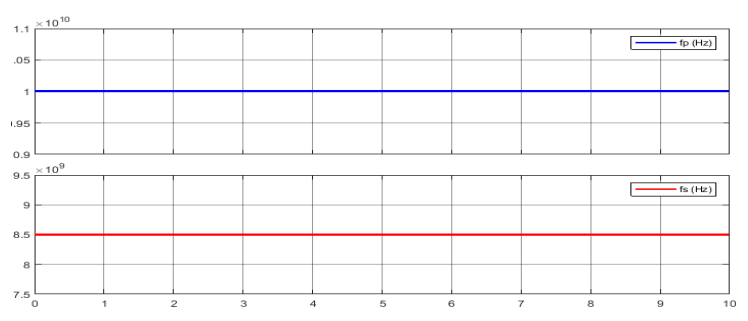


Fig. 13. The testing implementation results of the SPR-based MEMS design frequencies for fixed plasmon impedance parameters.

In Figure 13 above, it is clear that the variation of both the designed frequencies, fp and fs, will be constant (unchanged) with constant values of equivalent internal plasmonic impedances designed for the photocarrier model with the help of MEMS design properties and features. Moreover, the achieved SPR-based MEMS optical transmitted electromagnetic currents and voltages are shown in Figure 14 in the time domain.

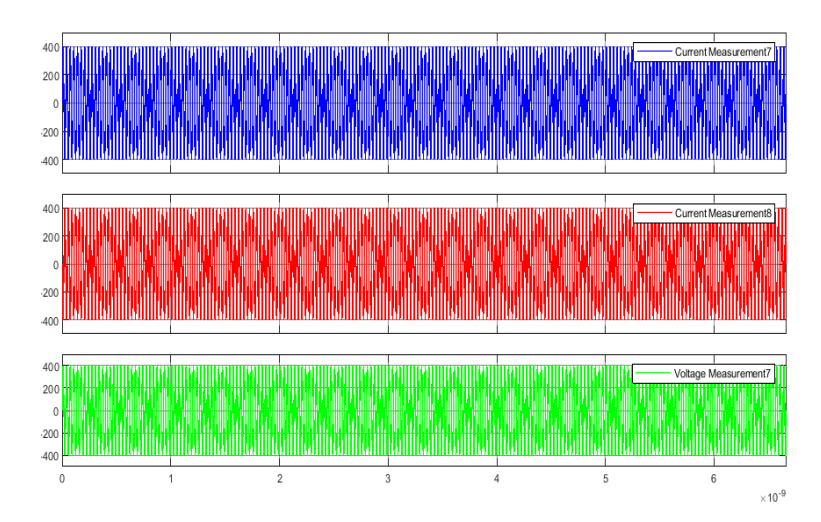


Fig. 14. The achieved SPR-based MEMS optical transmitted electromagnetic currents and voltages.

It is clear from Figure 14 that the obtained voltages and currents are alternating values with the vibrator design frequencies. It is also possible to note the high stability of the voltage and photoelectric current waves obtained from the design, which indicates the high performance efficiency of the design model of the SPR system based on the MEMS fiber sensor communication scheme. Furthermore, the spectral response of the resulting plasmon fiber model waveform is displayed in Figure 15.

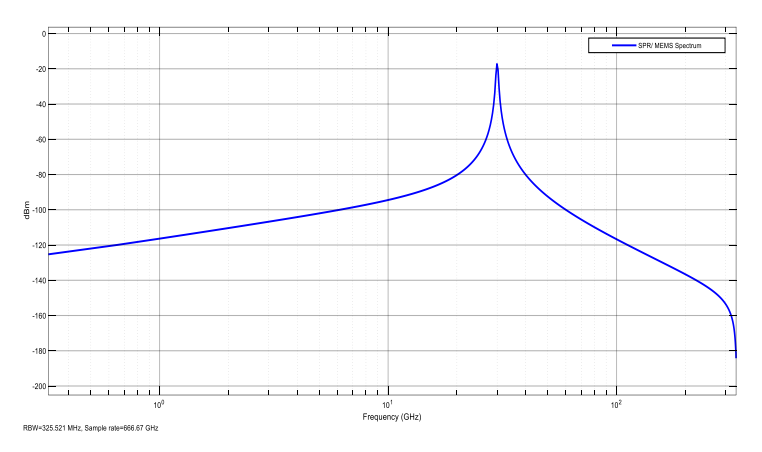


Fig. 15. The spectral response of the resulting plasmon fiber model waveform.

By regarding Figure 15, it might be noted that the result of the frequency spectrum of the simulated plasmonic optical carrier waveforms shows a high concentration of the spectrum of the proposed model within the design frequencies with a high amplitude of up to 20 dB, while all adjacent frequencies are efficiently suppressed, and the suppression power reaches 40 dB. This demonstrates the successful design of the proton optical carrier to act as a specific band filter.

As illustrated from the obtained test results, a percentage of changes in the initial capacitance C0, from 0-50%, will produce a decreasing response in the parallel frequency change of the SPR-based MEMS actuator, resulting from the self-test, Dfp, while the series frequency change, Dfs. It will have a continuous response without any effects. On the other hand, and referring to the results obtained, we may notice that the frequency response of the actuator of the SPR based MEMS model for the self-test to percentage changes of impedance in the motion amplitude, Cm, will be non-linear and inversely proportional to the series frequency change, Δfs , while for parallel frequency changes, Δfp , will handle a decreasing response up to 20% of the motion amplitude change, Cm, but beyond this range it will have a direct increasing response. As a result, the results of the self-test MEMS model actuator for percentage changes of Cm values and linear changes of impedance are shown in the results. The effect of percentage change in optical filter capacitance and resistance Cm on the designed resonant frequencies fp and fs is demonstrated in the achieved results. In this way, the change in the designed resonant frequency, fp, is inversely proportional to the percentage change in the vibrator amplitude Cm up to a 2% change, and then directly proportional to this change after a 3% change in the resonator amplitude and Cm change up to 10%. Moreover, as the simulation results show, there will be identical direct proportional changes in both the vibrator frequencies, fp and fs, for the percentage change in the resonator inductance Lm. Through a similar analysis, and referring to the results obtained, there will be no effect of the percentage change in the vibrator resistance, Rm, on the photocarrier modulation frequencies based on the MEMS design of the resonator, fp and fs. This is actually due to the physical properties represented by the equivalent mathematical equation defined for the filter configuration FBAR, which represents the relationship between Rm and fp, with the relationship fs. Finally, we observe the variation of the self-test MEMS actuator results affecting the designed

impedances C0, Cm, Lm, and Rm with respect to the ratio of the resonant frequencies, fp and fs. It is clear that the changes in the designed vibrator impedances, C0, Cm, Lm, and Rm, will be linearly and directly proportional to the percentage changes in the resonator frequencies, fp and fs. Consequences of the study can be developed more and more based on [XXV-XXXVIII].

V. Conclusion

In this review, implementations of modern plasmonic schemes utilized in ferromagnetic and nanomaterial-assisted optical communications are summarized. Their distinct roles are discussed in multiple ways, including beam focusing, routing, filtering, modulation, switching, detection, and filtering, all of which are of paramount importance for the advancement of 6G cellular networks. An optical communications system was simulated according to a SPR-based MEMS model that simulates the implementation and emply of plasmonic materials, relying on piezoelectronic filters such as electromagnetic resonators to filter optical waveforms and direct the communications beam efficiently and focused while reducing the data reception error rate to an excellent rate to avoid noise waves and interference for the sixth generation. The results showed an excellent response within the design specifications for working within a frequency band between 2 kHz and 2 THz, with stability remaining up to 50% change in equivalent impedance values to produce gain values of up to 20 dB at the design frequencies and a BER of up to -40 dB.

Conflict of Interest

The authors declare that there is no conflict of interest regarding this paper.

References

- I. Atabaki, A. H., Moazeni, S., Pavanello, F., Gevorgyan, H., Notaros, J., Alloatti, L., Wade, M. T., Sun, C., Kruger, S. A., Meng, H., et al. (2018). Integrating photonics with silicon nanoelectronics for the next generation of systems on a chip. Nature, 556, 349–354.
- II. Basak, C., Hosain, M. K., & Sazzad, A. A. (2020). Design and simulation of a high sensitive surface plasmon resonance biosensor for detection of biomolecules. Sensors & Imaging, 21, Article 1–19.
- III. Burla, M., Bonjour, R., Salamin, Y., Abrecht, F., Hoessbacher, C., Haffner, C., Heni, W., Fedoryshyn, Y., Baeuerle, B., Josten, A., et al. (2018). Plasmonics for next-generation wireless systems. In Proceedings of the 2018 IEEE/MTT-S International Microwave Symposium—IMS (Vol. 9, pp. 1308–1311). Philadelphia, PA, USA: IEEE.

- IV. Burla, M., Salamin, Y., Bonjour, R., Abrecht, F., Hoessbacher, C., Haffner, C., Heni, W., Fedoryshyn, Y., Werner, D., Baeuerle, B., et al. (2019). Integrated photonic and plasmonic technologies for microwave signal processing enabling mm-wave and sub-THz wireless communication systems. In Broadband Access Communication Technologies XIII (Vol. 1094505). San Francisco, CA, USA: SPIE.
- V. Chen, C., Mohr, D. A., Choi, H. K., Yoo, D., Li, M., & Oh, S. H. (2018). Waveguide-integrated compact plasmonic resonators for on-chip mid-infrared laser spectroscopy. Nano Letters, 18, 7601–7608.
- VI. Cohen, M., Abulafia, Y., Lev, D., Lewis, A., Shavit, R., & Zalevsky, Z. (2017). Wireless communication with nanoplasmonic data carriers: Macroscale propagation of nanophotonic plasmon polaritons probed by near-field nanoimaging. Nano Letters, 17, 5181–5186.
- VII. Chiu, N.F.; Lin, T.L.; Kuo, C.T. Highly sensitive carboxyl-graphene oxide-based surface plasmon resonance immunosensor for the detection of lung cancer for cytokeratin 19 biomarker in human plasma. Sens. Actuators B Chem. 2018, 265, 264–272.
- VIII. Diaz-Valencia, B. F., Mejía-Salazar, J. R., Oliveira, O. N., Jr., Porras-Montenegro, N., & Albella, P. (2017). Enhanced transverse magneto-optical Kerr effect in magnetoplasmonic crystals for the design of highly sensitive plasmonic (bio)sensing platforms. ACS Omega, 2, 7682–7685.
 - IX. Elder, D., Johnson, L., Tillack, A., Robinson, B. H., Haffner, C., Heni, W., Hoessbacher, C., Fedoryshyn, Y., Salamin, Y., Baeuerle, B., et al. (2018). Multi-scale theory-assisted nano-engineering of plasmonic-organic hybrid electro-optic device performance. In Organic Photonic Materials and Devices XX (Vol. 10529). San Francisco, CA, USA: SPIE.
 - X. Ghideli, M., Mascaretti, B., Bricchi, B. R., Zapelli, A., Russo, V., Casari, C. S., & Bassi, A. L. (2018). Engineering plasmonic nanostructured coverings by pulsed laser deposition. Applied Surface Science, 434, 1064–1073.
 - XI. Huang, Q.; Wang, Y.; Zhu, W.; Lai, T.; Peng, J.; Lyu, D.; Guo, D.; Yuan, Y.; Lewis, E.; Yang, M. Graphene-Gold-Au@Ag NPs-PDMS Films Coated Fiber Optic for Refractive Index and Temperature Sensing. IEEE Photonics Technol. Lett. 2019, 31, 1205–1208.
- XII. Hoessbacher, C., Josten, A., Baeuerle, B., Fedoryshyn, Y., Hettrich, H., Salamin, Y., Heni, W., Haffner, C., Kaiser, C., Schmid, R., et al. (2017). Plasmonic modulator with >170 GHz bandwidth demonstrated at 100 GBd NRZ. Optics Express, 25, 1762–1768.
- XIII. Kamran, M., & Faryad, M. (2018). Plasmonic sensor using a combination of grating and prism couplings. Plasmonics, 14, 791–798.
- XIV. Li, H., Chen, B., Qin, M., & Wang, L. (2020). Strong plasmon-exciton coupling in MIM waveguide-resonator systems with WS2 monolayer. Optics Express, 28, 205–215.

- XV. Li, T., Zhu, L., Yang, X., Lou, X., & Yu, L. (2020). A refractive index sensor based on H-shaped photonic crystal fibers coated with Ag-graphene layers. Sensors, 20, 741. 10.3390/s20030741
- XVI. Mejía-Salazar, J. R., Camacho, S. A., Constantino, C. J. L., & Oliveira, O. N., Jr. (2018). New trends in plasmonic (bio)sensing. Anais da Academia Brasileira de Ciências, 90, 779–801.
- XVII. Mejía-Salazar, J. R., & Oliveira, O. N., Jr. (2018). Plasmonics biosensing. Chemical Reviews, 118, 10617–10625.
- XVIII. Muench, J. E., Ruocco, A., Giambra, M. A., Miseikis, V., Zhang, D., Wang, J., Watson, H. F. Y., Park, G. C., Akhavan, S., Midrio, M., et al. (2019). Waveguide-integrated, plasmonic enhanced graphene photodetectors. Nano Letters, 19, 7632–7644.
 - XIX. Pitelet, A., Mallet, E., Ajib, R., Lemaître, C., Centeno, E., & Moreau, A. (2018). Plasmonic enhancement of spatial dispersion effects in prism coupler experiments. Physical Review B, 98, 125418.
 - XX. Sadeghi, Z., & Shirkani, H. (2020). Highly sensitive mid-infrared SPR biosensor for a wide range of biomolecules and biological cells based on graphene-gold grating. Physica E: Low-Dimensional Systems and Nanostructures, 119, 114005.
 - XXI. Salaliya, P. B., Gupta, N., & Dhawan, A. (2019). Steerable plasmonic nanoantennas: Active steering of radiation patterns using phase change materials. Optics Express, 27, 31567–31586.
- XXII. Savaliya, P. B., Gupta, N., & Dhawan, A. (2019). Steerable plasmonic nanoantennas: Active steering of radiation patterns using phase change materials. Optics Express, 27, 31567–31586. [Note: duplicate entry consolidated if desired]
- XXIII. SBrT Zúñiga, D. J. C., Mafra, S. B., Mejía-Salazar, J. R., Montejo-Sánchez, S., Fernandez, E. M. G., & Céspedes, S. (2019). Visible light V2V cooperative communication under environmental interference. SBrT. 10.14209/SBRT.2019.1570558276
- XXIV. Thraskias, C. A., Lallas, E. N., Neumann, N., Schares, L., Offrein, B. J., Henker, R., Plettemeier, D., Ellinger, F., Leuthold, J., & Tomkos, I. (2018). Survey of photonic and plasmonic interconnect technologies for intra-datacenter and high-performance computing communications. IEEE Communications Surveys & Tutorials, 20, 2758–2783.
- XXV. Ummethala, S., Harter, T., Koehnle, K., Muehlbrandt, S., Kutuvantavida, Y., Kemal, J., Marin-Palomo, P., Schaefer, J., Tessmann, A., Garlapati, S. K., et al. (2019). THz-to-optical conversion in wireless communications using an ultra-broadband plasmonic modulator. Nature Photonics, 13, 519–524.
- XXVI. Wei, H., Pan, D., Zhang, S., Li, Z., Li, Q., Liu, N., & Xu, H. (2018). Plasmon waveguiding in nanowires. Chemical Reviews, 118, 2882–2926.
- XXVII. Yoo, K., Becker, S. F., Silies, M., Yu, S., Lienau, C., & Park, N. (2019). Steering second-harmonic radiation through local excitations of plasmon. Optics Express, 27, 18246–18261.

- XXVIII. Yaqeen S.Mezaal, Halil T. Eyyuboğlu, and Jawad K. Ali. "New microstrip bandpass filter designs based on stepped impedance Hilbert fractal resonators." IETE Journal of Research 60.3 (2014): 257-264..
 - XXIX. Y. S. Mezaal, L. N. Yousif, Z. J. Abdulkareem, H. A. Hussein, and S. K. Khaleel, "Review about effects of IoT and nanotechnology techniques in the development of IoNT in wireless systems," *International Journal of Engineering and Technology*, vol. 7, no. 4, pp. 3602–3606, 2018. 10.14419/ijet.v7i4.19615...
 - XXX. Yahya, A., J. A. Aldhaibaini, R. B. Ahmad, Z. G. Ali, and R. A. Fayadh, "Enhancing link quality in a multi-hop relay in LTE-A employing directional antenna," in 2013 IEEE International RF and Microwave Conference (RFM), 2013. 10.1109/RFM.2013.6757227
 - XXXI. Yahya, A., J. A. Aldhaibaini, R. B. Ahmad, M. Zain, and A. S. Salman, "PERFORMANCE ANALYSIS OF TWO-WAY MULTI-USER WITH BALANCE TRANSMITTED POWER OF RELAY IN LTE-A CELLULAR NETWORKS," Journal of Theoretical & Applied Information Technology, vol. 51, no. 2, 2013.
- XXXII. Zainab Falih Hamza, et. al. "Estimating systems reliability functions for the generalized exponential distribution with application", *Period. Eng. Nat. Sci.*, vol. 11, no. 3, pp. 108–114, May 2023, 10.21533/pen.v11.i3.138
- XXXIII. Zhang, Muench? (entry merged) Muench, J. E., Ruocco, A., Giambra, M. A., Miseikis, V., Zhang, D., Wang, J., Watson, H. F. Y., Park, G. C., Akhavan, S., Midrio, M., et al. (2019). Waveguide-integrated, plasmonic enhanced graphene photodetectors. Nano Letters, 19, 7632–7644.
- XXXIV. Zia, R., Schuller, J. A., Chandran, A., & Brongersma, M. L. (2006). Plasmonics: The next chip-scale technology. Materials Today, 9, 20–27.
- XXXV. Zhu, J., Xu, Z., Xu, W., Fu, D., & Wei, D. (2018). Surface plasmon polariton waveguide by bottom and top of graphene. Plasmonics, 13, 1513–1522.
- XXXVI. Zhu, J., & Xu, Z. (2019). Tunable temperature sensor based on an integrated plasmonic grating. Optical Materials Express, 9, 435–440.
- XXXVII. Zhou, X.; Li, X.; Cheng, T.L.; Li, S.; An, G. Graphene enhanced optical fiber SPR sensor for liquid concentration measurement. Opt. Fiber Technol. **2018**, 43, 62–66
- XXXVIII. Zhuang, T., Li, S., Song, G., Jiang, P., & Yu, L. (2019). Tunable band-stop plasmonic waveguide filter with single-sided multiple-teeth-shaped structure. Physica Scripta, 94, 095602.